High Aspect Ratio Multi-Stage Ducted Electroaerodynamic Thrusters for Micro Air Vehicle Propulsion

C. Luke Nelson and Daniel S. Drew

***Abstract*—Electroaerodynamic propulsion, where force is produced through collisions between electrostatically accelerated ions and neutral air molecules, is an attractive alternative to propeller- and flapping wing-based methods for micro air vehicle (MAV) flight due to its silent and solid-state nature. One major barrier to adoption is its limited thrust efficiency at useful disk loading levels. Ducted actuators comprising multiple serially-integrated acceleration stages are a potential solution, allowing individual stages to operate at higher efficiency while maintaining a useful total thrust, and potentially improving efficiency through various aerodynamic and fluid dynamic mechanisms. Here, we investigate the effects of duct and emitter electrode geometries on actuator performance, then show how a combination of increasing cross-sectional aspect ratio and serial integration of multiple stages can be used to produce overall thrusts comparable to state-of-the-art flapping wing robots. A five-stage device is shown to reach a thrust density of about 18 N/m^2, an order of magnitude higher than what has previously been achieved at this scale, with the same measured thrust efficiency as reported in prior work. We also show how a high aspect ratio multi-stage ducted thruster could be integrated under the wings of a MAV-scale platform, pointing towards use as a distributed propulsion system in future work.**

***Index Terms*—Micro/nano robots, aerial systems: mechanics and control, actuation and joint mechanisms.**

I. Introduction

AUTONOMOUS micro air vehicles (MAVs) are poised to transform the way that we gather information from the world around us. Whether it is in commercial, industrial, or defense settings, the ability to unobtrusively collect data using cheap, high agent count systems would be highly beneficial [1], [2]. Accordingly, academic research on MAV platforms ranging from fixed-wing gliders to bio-inspired flappers has grown steadily since the early 2000s [3]. The science of autonomy at small scales has also advanced: sub-gram electronics payloads are now sufficient for flight control [4], untethered flight of insect-scale robots has been shown with beamed power [5], and groups of MAVs have been shown working together in unstructured environments [6].

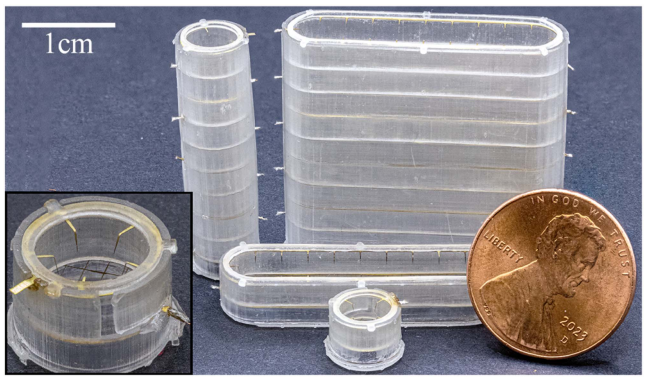

Fig. 1. Multi-stage ducted electroaerodynamic thrusters next to U.S. penny for scale: a 6 mm diameter five-stage cylindrical thruster (back left), a five-stage aspect ratio five thruster (back right), and single stage versions in front of them. Inset: Closer view at a single cylindrical stage showing the five emitter tips bent vertically down towards a collector grid.

Current commercial rotor-based MAVs, however, are not suitable for all types of envisioned deployments. Fundamental challenges like the poor aerodynamic efficiency of small propellers and the decreased performance of miniaturized electromagnetic motors means that centimeter-scale quadrotors are often limited to flight times on the order of minutes [7]. In addition, their propellers, spinning at tens of thousands of RPM, are fragile and noisy, making them unlikely to be useful in human-proximal and space-constrained environments [8]. To overcome these challenges, researchers have turned towards biomimetic flapping-wing designs, which exhibit better aerodynamic scaling at low Reynolds numbers [9]. Nevertheless, their demonstrated lift efficiency and achievable thrust-to-weight ratio have still yet to exceed that of a quadrotor, and the motion of their wings relies on complicated transmissions [10]. Atmospheric ion thrusters (Fig. 1) are an attractive alternative, especially for fixed-wing and lighter-than-air fliers which are not easily outfitted with flapping wings.

Electrohydrodynamic (EHD) propulsion, where force is produced via the momentum-transferring collisions of ions with neutral fluid molecules, works virtually silently and with no mechanical moving parts. When the impacted neutral molecules are atmospheric air, it is known as electroaerodynamic (EAD) propulsion. EAD thrusters have propelled platforms ranging from a five-meter wingspan "solid-state aeroplane [11]" to the

Manuscript received 2 August 2023; accepted 26 December 2023. Date of publication 18 January 2024; date of current version 8 February 2024. This letter was recommended for publication by Associate Editor J. Liu and Editor X. Liu upon evaluation of the reviewers' comments. *(Corresponding author: Daniel S. Drew.)*

C. Luke Nelson is with the Department of Mechanical Engineering, University of Utah, Salt Lake City, UT 84112 USA (e-mail: charles.nelson@utah.edu).

Daniel S. Drew is with the Department of Electrical and Computer Engineering, University of Utah, Salt Lake City, UT 84112 USA (e-mail: daniel.drew@utah.edu).

Digital Object Identifier 10.1109/LRA.2024.3355728

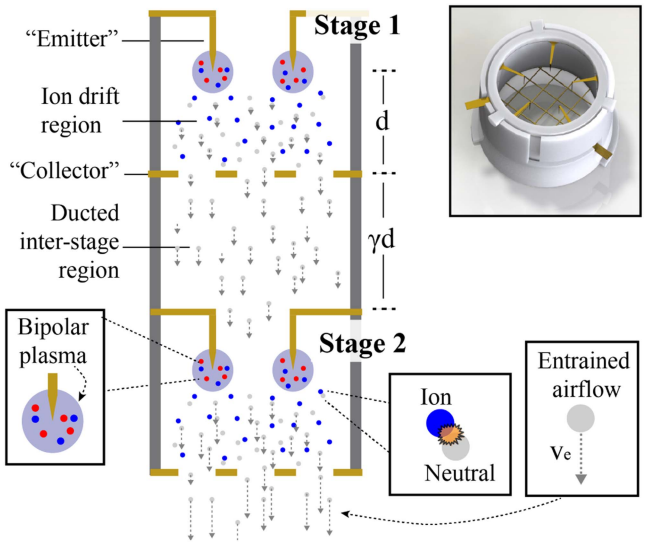

Fig. 2. Schematic view of a two-stage ducted electroaerodynamic thruster in cross section. Ions are ejected from the bipolar corona plasma locally confined to the volume around the emitter tips and drift towards the collector grid under the influence of an applied electric field. Along the way, they collide with neutral air molecules and transfer their momentum, resulting in an entrained airflow through the collector grid.

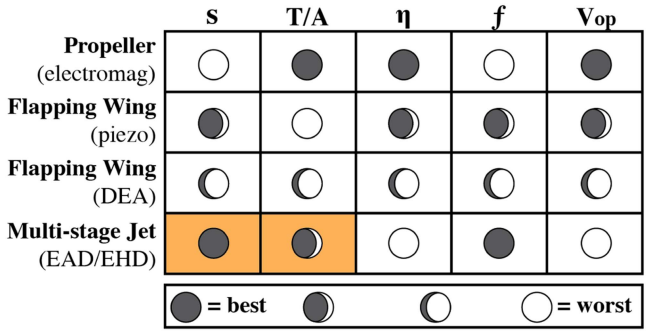

Fig. 3. Qualitative comparison of different micro air vehicle propulsion strategies based on values gathered and calculated from [7], [9], [10], [18]. Here **s** refers to size down-scalability, **T/A** is thrust density, \boldmath η is thrust efficiency, f is airfoil frequency, and V_{op} is operating voltage. The orange cells refer to the specific contribution of this work.

insect-scale "ionocraft [12]." It is particularly well suited for miniaturization and use in MAVs due to its cross-sectional force scaling, simple mechanical design amenable to batch manufacturing, and ability to modulate force directly with applied voltage. Corona discharge (Fig. 2) is the most common mechanism for ion generation in EAD actuators owing to its simplicity (e.g., a single applied potential both strikes the plasma and accelerates the ions) and for its proven reliability (e.g., it is often used as a stable ion source for spectroscopy).

The fundamental physical phenomena governing electroaerodynamic propulsion are well understood for simple cases; at its core, performance is governed by the electric drift field magnitude accelerating the ions for their collisions with neutral air molecules [13]. There is an inherent trade off between force and efficiency established by validated theory, with bounding values for each coarsely determined by the breakdown field in air and the space charge limit for unipolar drift current [14], [15]. A one-dimensional derivation yields equations for force, F, and thrust efficiency in N/W, η, as functions of electric field, ion drift current and travel distance, and ion mobility μ [13]:

$$F = \frac{Id}{\mu} = \frac{9}{8}\epsilon_0 A E^2 \tag{1}$$

$$\eta = \frac{1}{\mu E} \tag{2}$$

While these equations do not capture various loss factors specific to individual device geometries and ion generation mechanisms, it is clear that there is an inherent trade-off between thrust and thrust efficiency as dictated by the ion drift field magnitude. One method proposed to overcome this fundamental tradeoff—to produce actuators with both high thrust density and high efficiency—is to stack many small acceleration stages in series in a single "multi-stage ducted (MSD)" device [16], [17]. Each stage can be driven at a higher efficiency and lower thrust operating point, then multiple stages can be used to reach the total desired force output (and increase the total effective thrust density). Ducting the serially-integrated acceleration stages (Fig. 2) is a way to reduce losses, effectively package propulsors, and even improve overall efficiency via aerodynamic mechanisms like pressure forces acting on the duct [17]. This multi-stage approach is especially amenable to miniaturization, as volumetric force density of an EAD device is related to its inter-electrode gap, whereas force and efficiency are governed by the scale invariant electric field magnitude. This means that in a given actuator volume, using multiple miniaturized stages instead of a single one can increase power density without affecting areal thrust or thrust efficiency.

The broad objective of this work is to investigate centimeter-scale multi-stage ducted EAD thrusters and provide a feasibility proof for their use in MAV propulsion. They are compared qualitatively to other alternatives in Fig. 3; in this study, we focus on proving that they can be both miniaturized and scaled to meet design constraints, and that they can achieve high thrust densities.

The specific contributions of this work include an empirical study of emitter electrode and duct geometric parameters, a demonstration of how scaling annular thrusters to high aspect ratios can increase force without compromising thrust density or efficiency, and characterization of multi-stage devices with more stages than have ever been shown at this scale. We include simple models as a starting point for future design optimization. Our devices, which achieve an order-of-magnitude higher thrust density than any other EAD propulsive device to date, point the way towards autonomous MAVs with distributed EAD propulsion in the future.

II. Related Work

A. EAD Propulsion for Flying Robots

EAD-based distributed propulsion for unmanned fixed-wing flight was shown at the meter-scale by Xu et al. [11], but used unducted actuators two orders of magnitude larger than in this work. Microfabricated silicon electrodes have been

used to produce high (≈10) thrust-to-weight ratio centimeter scale fliers [19], and an EAD quad-thruster design has lifted a useful sensor payload with tethered power [12]. Ductless single-stage actuators using UV laser microfabricated electrodes (as in this work) have been shown to produce sufficient thrust for liftoff [20], [21], [22].

B. Ducted EAD Actuators

While the majority of effort on EAD propulsion has focused on ductless designs, there is existing work studying single- and multi-stage ducted devices for the more general purpose of maximizing volumetric flow rate for fluid pumping. Kim et al. found that exhaust velocity and electromechanical efficiency increased with the square root of the number of active stages (from one to six) for a straight ducted device 78 mm in diameter [23]. Rickard et al. [24] found a parabolic increase in dynamic pressure with increasing active stage count, and attributed that to friction losses. In each case, presented models for performance are based on curve-fit hyperparameters to their experimental data. Here, we investigate much smaller devices, at lower Reynolds numbers, with significantly different electrode geometries, which require their own parameter derivations.

Moreau et al. showed that electromechanical efficiency of an EHD pump was reduced when duct size was too small relative to the inter-electrode gap, with a local maximum at some diameter between one and two times the gap [25]. Here we focus instead on how the relationship between inter-electrode, emitter-to-duct, and emitter-to-emitter spacing affect discharge and aerodynamic performance.

Research on ducted EAD devices for propulsion is still new. Drew et al. found a near linear increase in output force with number of stages (from one to three) in a millimeter-scale device, but did not thoroughly investigate emitter design parameters or duct geometry [16]. Gomez-Vega et al. [17] presented an analytical model for multi-stage ducted EAD devices based on simple momentum theory, which shows the potential for orders of magnitude improvement in thrust at a given thrust efficiency (or vice versa) depending on inter-stage losses. While they focus on collector drag from individual wire-wire pairs, we focus on multi-point-to-grid geometries, discuss the importance of frictional losses in the duct in more detail, and provide experimental validation.

For rotor-propelled craft, ducting has been shown to increase thrust up to 50% higher than when open [26], and a 6.5 cm diameter shrouded rotor has been shown to reduce power requirements for hovering by about 10% [27]. The aerodynamics of EAD propulsors are sufficiently different (e.g., there are no tip vortices) to warrant focused study.

III. Methods and Approach

A. Electrode Design

Electrodes are fabricated with a 355-nm UV laser micromachining system (DPSS Samurai) to etch 25 μm thick brass shim stock. Duct structures are fabricated via stereolithographic printing (Formlabs Form 3+, clear resin).

Prior work showed that lithographically-defined emitter asperities can reduce corona onset voltage and increase subsequent ion current compared to a bare wire [28]. Here, we define emitter tips lithographically and arrange them inwards from an annulus or rounded rectangle, depending on the device aspect ratio. Each emitter tip is drawn as a triangle with a height defined by the difference in diameters between the outer circle where the triangles begin, d_2, and an inner circle where their tips reach, d_1. Each emitter tip is bent downwards 1 mm at a right angle where it meets the edge of the inner circle, yielding a distance from the tip to the annulus lip of $\sqrt{(d_2 - d_1)^2 + 1}$. The field enhancement factor of the emitter tips, responsible in part for determining the corona discharge performance, results from a combination of the effective radius of curvature of the tip after etching and electrostatic shielding from the metal rim of the electrode and from neighboring emitter tips. Preliminary process development determined the minimum nominal tip angle repeatably achievable in the UV laser micromachining process to be 5°, which is used for all emitters. All devices use a 2 mm inter-electrode (emitter tip to collector grid) gap.

Based on prior success with point-to-grid designs and a desire to focus on emitter effects in this work, we opted for a grid collector geometry. The collector grids must balance presenting a quasi-uniform potential plane in order to maximize discharge performance with the desire to minimize aerodynamic drag on the air which is accelerated through it via ion-neutral collisions. Preliminary results found that grids with a wire width of 50 μm and a wire spacing of 1 mm had no effect on corona onset voltage compared to less sparse designs, and were able to be repeatability fabricated and assembled. This agrees with prior work, which found that a grid spacing equal to approximately half the inter-electrode distance did not influence discharge performance [28].

B. Fabrication and Assembly

Reliable fabrication and assembly is seen as one of the major barriers to progress in novel micro (and smaller) air vehicle development [9]. Producing millimeter-scale EAD actuators, which still operate at high voltage, is particularly challenging given their tendency to destructively arc. Integrating multiple stages further compounds error from device variability, limiting attainable stage count [16]. We have developed a new methodology to produce modular millimeter-scale actuators based on SLA printed and UV laser microfabricated components which results in high yield and low variability (Fig. 4).

The annular emitter design used here requires the emitters to be bent out of plane towards the collector grid. We accomplish this using an SLA-printed stamp and die set to hold the annulus in place while plastically deforming the tips; the emitter electrode is then lifted out of the die and placed into the final device duct. A rotating tab design and a two-layer sleeve system means that no adhesive is required to fix the electrodes in place relative to the three duct components.

The individual stages must be separated by some distance to minimize electrostatic interference (e.g., between the collector electrode of the first stage and the emitter electrode of the second), which can degrade corona discharge performance (see Fig. 2). Although Gilmore et al. determined a rough heuristic – that the inter-stage gap should be about twice the inter-electrode gap in order to maximize performance [15]– this was only validated using wire-to-cylinder electrode geometries. We print

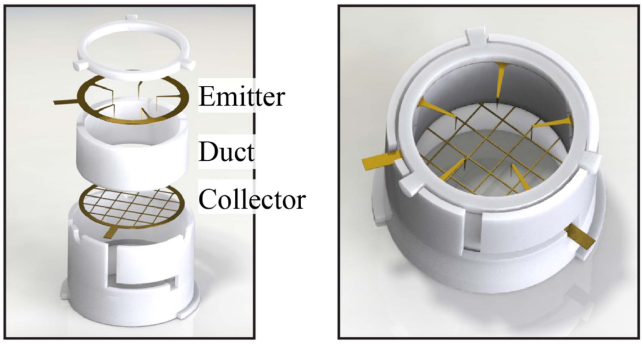

Fig. 4. Rendered view of the ducted electroaerodynamic thrusters used in this work, with individual components separated to show the assembly process. Laser micromachined active electrodes are integrated with SLA-printed duct structures in an adhesiveless process based on precise mechanical affordances. Prior to insertion in the duct, emitter electrodes are bent out of plane using an SLA-printed stamp and die set (not shown).

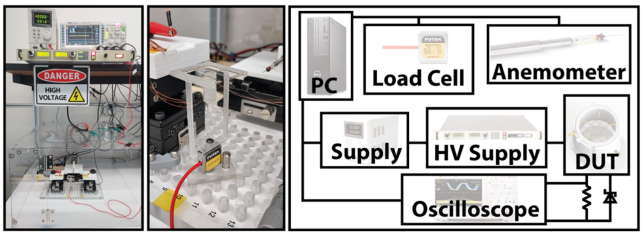

Fig. 5. Pictures (left) and block diagram (right) of the experimental setup used for automated data acquisition.

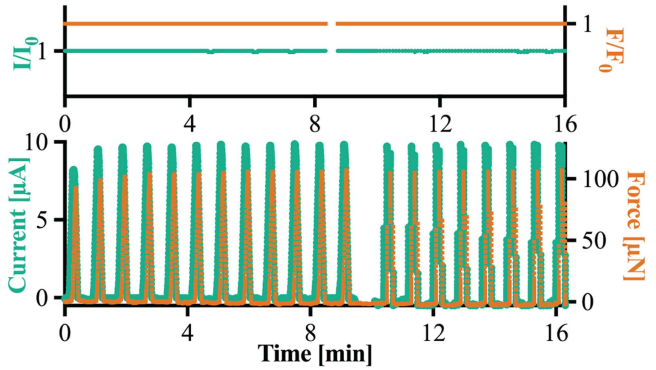

Fig. 6. Three-stage aspect ratio one device current and force as a function of time to show stability during discharge. Device operated at 3 kV.

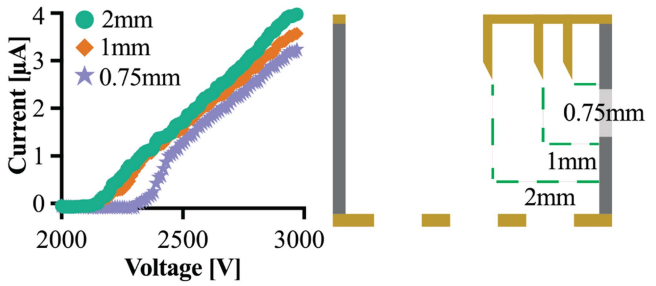

Fig. 7. Current-voltage curves for 6 mm inner diameter devices with one emitter tip, with decreasing lateral distances of 2 mm, 1 mm, 0.75 mm (2.23 mm, 1.41 mm, and 1.25 mm, radially) from the annulus inner lip.

a variable length ducted inter-stage section which is included in the adhesiveless assembly process to investigate this further.

C. Experimental Methodology

The device under test is fixed to a laser-cut polyetherimide (PEI) slide which can be used for either force or outlet air velocity measurement. Voltage is digitally controlled through a Spellman High Voltage SL8P supply. The ion current is measured via oscilloscope across a TVS diode-protected shunt resistor. A hot wire anemometer (TSI 8465) is mounted to a motorized X/Y stage for multi-point velocity measurements. Force measurements are made using a printed test stand on a FUTEK LSB200 S-Beam load cell, with the actuator elevated to reduce possible proximity effects. Everything is fixed to a plastic optical breadboard. Images and a diagram of the experimental setup are shown in Fig. 5.

IV. Experiments and Results

All experiments are performed with three devices per test condition and three trials per device. Plotted data is the overall mean (mean of each device's trial mean) with standard error of the mean (SEM) error bars.

A. Device Lifetime

We characterized device lifetime to assess the ability of our brass micromachined electrodes to withstand the energetic corona plasma. Fig. 6 shows the current and force output for a three-stage aspect ratio one device over a 1000 s period, either operated at a constant 3 kV or with repeated corona plasma inception cycling, with no observed performance change. We continued the discharge cycling experiment to over 100 cycles (not shown on graph, for clarity) without observable change.

B. Duct Size and Emitter Geometry

We conducted experiments to investigate the hypothesis that the minimum distance between emitter tips to prevent performance degradation is related to the space charge repulsion radius r predicted by the Warburg law for a specific inter-electrode gap, $r = arctan(\pi/3)d$ [29]. This corresponds to a radius of 1.6 mm for the 2 mm gap used here. Emitter tips located closer to the duct edge than this distance, or closer than twice this distance to a neighboring emitter tip, are expected to show increased onset voltage and decreased ion current [25].

Discharge from a single emitter tip with variable distance from the annulus lip (Fig. 7) showed a decreased maximum current but not a significant onset voltage change for 1 mm lateral distance, which corresponds to a 1.4 mm radial distance based on the hypotenuse from the tip (bent 1 mm down) and the lip. The onset voltage increased significantly (≈200 V) for the 0.75 mm (1.25 mm hypotenuse) condition.

Experiments conducted with multi-emitter configurations for both 6 mm and 8 mm inner diameters (Fig. 8) showed the expected onset voltage increase with more emitters (i.e., a decreased distance between emitters for a fixed inner diameter). In Fig. 9, we show the measured thrust density versus number

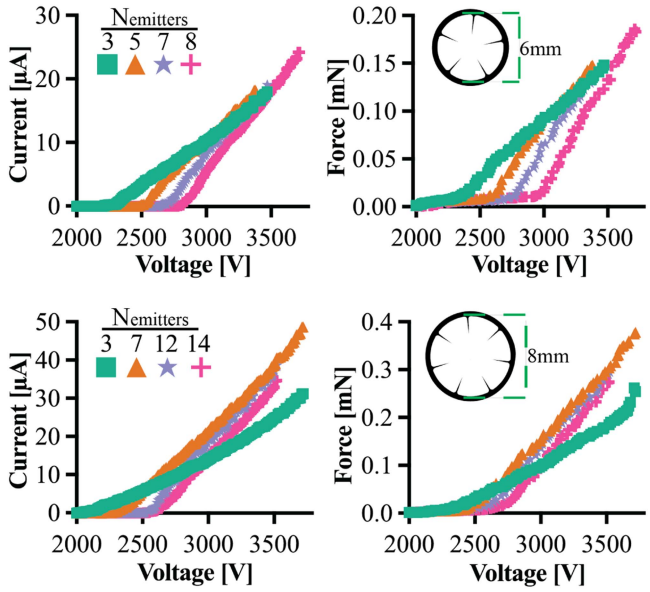

Fig. 8. Current-voltage and force-voltage curves for single stage 6 mm (top) and 8 mm (bottom) inner diameter devices with different numbers of emitter tips. The 6 mm three emitter condition corresponds to a tip-to-tip distance of approximately 3.5 mm, while the five emitter distance is below the expected interference threshold from the Warburg law at only 2.3 mm.

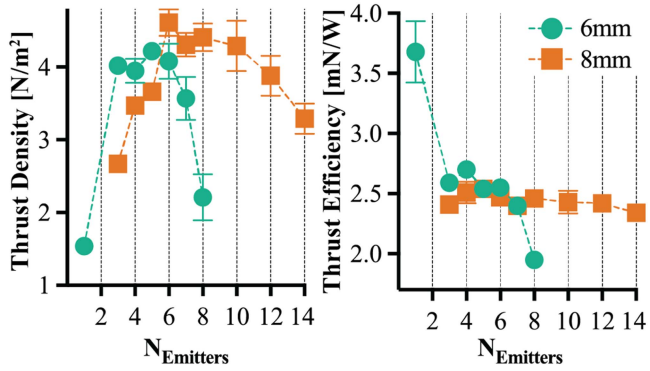

Fig. 9. Thrust density and thrust efficiency versus number of emitter tips for different duct inner diameters. All data collected at 3.2 kV applied voltage; note that this is at the upper end of these devices' operating range, where the highest thrust density and lowest efficiency is expected.

of emitters reaches a local maximum before decreasing as the emitters become closer together.

We show the discharge current is a strong function of the voltage as well as the ratio between the distance between the emitter tips and the inter-electrode gap, κ (3). Fig. 10 shows the marginal increase in current and force per emitter versus κ, which decreases as number of emitters increases for a constant inner duct diameter. Corona discharge performance can be captured by the simple relation given in (4) with geometric hyperparameter C, noting that both C and V_0 are actually functions of κ [30].

$$\kappa = \frac{d_{ee}}{d_{ec}} = \frac{d_i sin(\pi/N_E)}{2} \tag{3}$$

$$I_1 = C(\kappa)V(V - V_0(\kappa)) \tag{4}$$

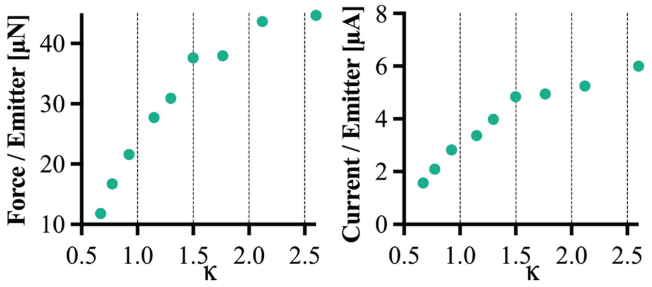

Fig. 10. Marginal increase in force (left) and current (right) as functions of κ, which decreases with additional emitters for a constant annulus diameter. Data for 8 mm aspect ratio three devices.

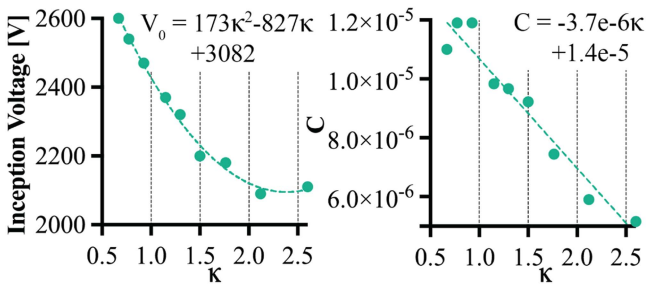

Fig. 11. Corona onset voltage V_0 (found where the current reaches 0.5 μA) and discharge hyperparameter C as functions of κ, with polynomial and linear fit functions. Data for 8 mm aspect ratio three devices.

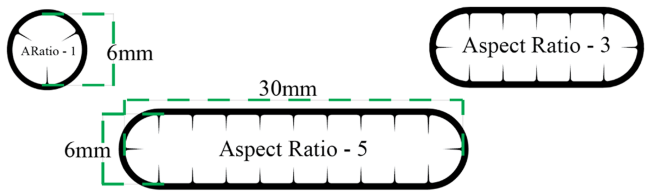

Fig. 12. Schematic illustration of increasing emitter electrode aspect ratio, including a 6 mm inner diameter aspect ratio one (i.e., circular) electrode (top left), an 18 mm by 6 mm aspect ratio three device (top right), and an aspect ratio five electrode with dimensions labeled (bottom).

We fit functions for C and V_0 to our experimental data in Fig. 11. These can be used for constraint-driven design and optimization in future work, noting that they are only valid for this specific annular thruster geometry.

C. Aspect Ratio

For an annular thruster, it is evident that simply scaling the device diameter is not an effective way to increase output force; circumferential emitters are arrayed optimally based on inter-electrode gap, not diameter, and thus the center of the annulus is increasingly "wasted" area. We hypothesized that since the 6 mm diameter device has a nominal tip-to-tip distance across its diameter of 4 mm for the 1 mm lateral placement condition (more than that necessitated by the Warburg law), elongating the duct to a higher aspect ratio (see Fig. 12) while retaining an emitter-to-emitter distance of ≈3 mm along its circumference would result in a higher achievable force output without decreasing areal thrust.

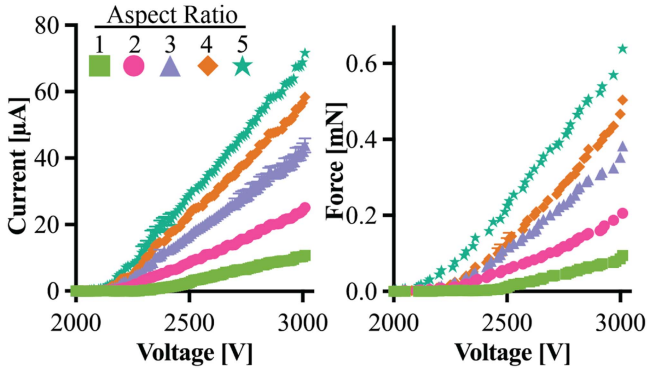

Fig. 13. Current-voltage and force-voltage curves for single stage aspect ratio one through five thrusters based on the 6 mm diameter emitter-emitter-distance of 3 mm, 2 mm inter-electrode gap base design.

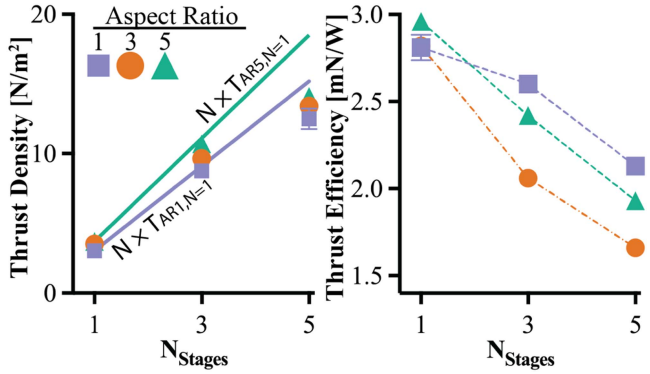

Fig. 14. Thrust and thrust efficiency versus thruster aspect ratio, defined as w/h where a circular duct of diameter 6 mm is an aspect ratio of one. For aspect ratios above one, emitter tips are placed to maintain approximately the same circumferential distance as in the aspect ratio one device. All data collected at 3 kV applied voltage with an inter-electrode gap of 2 mm. Solid lines represent a linear extrapolation from single-stage thrust density.

Fig. 13 shows the current-voltage and force-voltage for single-stage devices with aspect ratios ranging from one (i.e., a circle) to five. The number of emitters for each aspect ratio is the aspect ratio multiplied by four (e.g., aspect ratio five has 20 emitters). We see a near linear increase in total output force with increasing aspect ratio, indicating that our device scaling methodology was successful. Fig. 14 shows that the thrust and thrust efficiency remain approximately constant as the aspect ratio increases from one to five for a single stage. The data for stage counts above one are discussed later.

D. Inter-Stage Length

One of the challenges with multi-stage devices is managing the electrostatic interactions between active electrodes in neighboring stages (e.g., the collector of stage one and the emitter of stage two). We investigated the hypothesis that our device structure would allow us to decrease the interstage distance ratio below 2 d, a value experimentally determined in prior work by Gilmore et al. [15] and Drew et al. [16], because the annular bent emitters effectively shields the tips from the preceding stage.

Fig. 15 shows results for the inter-stage distances of 2 d, 1.5 d, and d, which exhibit near identical performance in a two-stage

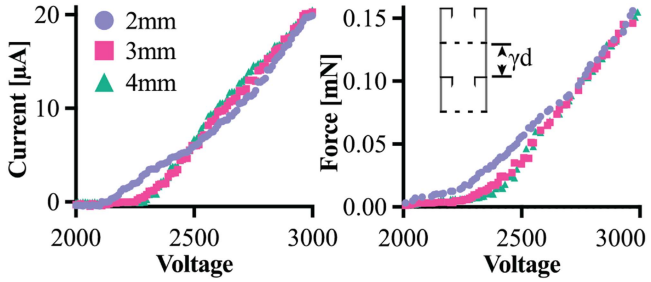

Fig. 15. Results for variable inter-stage distances of 2 mm, 3 mm, and 4 mm, corresponding to γ values of 1, 1.5, and 2.

device above about 2750 V. Below d, arcing along the duct surface between the outer edges of the emitter and collector was the limiting factor. Onset voltage appears to *decrease* for the 2 mm (1 d) condition. Some devices would arc between the collector of stage one and the bent corners of the stage two emitters prior to discharge (data from those "failed" devices not shown). The decreased onset voltage and interesting shape of the IV curve could possibly be attributed to reverse corona discharge from the emitter corners to the prior collector, with some percentage of that plasma's ejected ions actually drifting towards the "correct" collector. To remove this unpredictable element we performed all subsequent experiments at an inter-stage gap of 3 mm (1.5 d).

E. Stage Count

Prior work on multi-stage ducted EAD devices exhibited sub-linear scaling of output force with number of stages [16]. Our hypothesis was that the careful process control we took for developing low-friction duct wall surfaces would reduce inter-stage losses. Conversely, preliminary modeling showed that the flow would fail to fully develop in the duct lengths shown here at the low Reynolds numbers achievable by these devices, especially given the turbulence induced by passage through the collector grids. We therefore expected no efficiency benefit as may have been predicted by recent analytical modeling efforts [17].

Fig. 14 shows the thrust efficiency acutely drops with an increase in stages. A possible explanation is that efficiency losses are largely due to frictional losses in the inter-stage region (see Fig. 2) arising due to turbulence generated from the collector grid and the additional duct surface area. This loss causes increased deviation from the density that would be predicted for multiple stages given a linear fit (see the $N \times T$ lines in Fig. 14). This can also be seen in Fig. 16, where the linear increase in current with number of stages would yield a linear increase in force (via (1)) if not for drag/frictional losses.

Fig. 17 shows outlet air velocity data measured from one-stage and five-stage aspect ratio three devices via a hot wire anemometer. The characteristic convergent jet plume expected from a ducted actuator is evident in both cases, indicating that models for fluid dynamic/aerodynamic efficiency gains hypothesized for circular ducted actuators should extend to high aspect ratio devices. Taking the 6 mm axis as the chord length, the Reynolds number for the five-stage device is approximately 2000, falling in the transition region from laminar to turbulent flow where analytical models often fail.

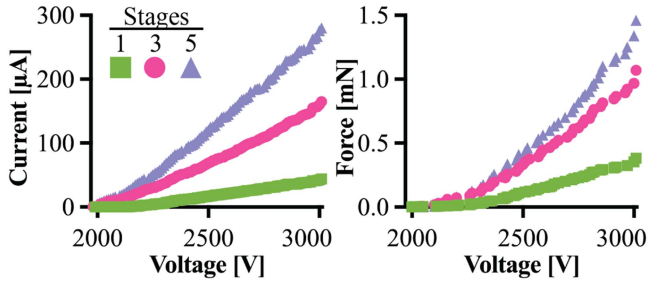

Fig. 16. Discharge current (left) and force (right) as a function of voltage for aspect ratio three thrusters with one, three, and five stages.

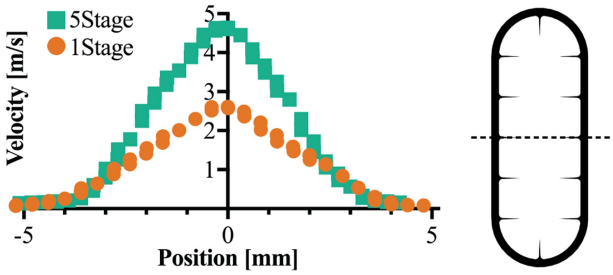

Fig. 17. Two dimensional air velocity data measured at the outlet of one-stage and five-stage aspect ratio three thrusters.

Our data supports the formation of a simple analytical model for total output force as a function of stage count, aspect ratio, and κ. In general, the total force can be described by a combination of the electrostatic force, the form drag, and the skin friction drag (5).

$$F = F_{es} - F_{fd} - F_{sf} \tag{5}$$

The surface area of the inner duct as a function of aspect ratio and stage count (7) and the area of the collector grid as a function of aspect ratio and grid open area fraction can be found using simple geometry (8).

$$S_d(AR) = 2\pi r_i(d_{ec}+1) + 2(AR-1)d_i(d_{ec}+1) \tag{6}$$

$$S_d(AR,N) = NS_{AR} + (N-1)\frac{\gamma d_{ec}}{d_{ec}+1}S_{AR} \tag{7}$$

$$A_c(AR) = OOF(\pi r_i^2 + 4r_i^2(AR-1)) \tag{8}$$

These equations can be combined with canonical expressions for drag force and EAD electrostatic force (1) to yield an equation for total force in a similar form to that presented by Gomez-Vega et al. [17], but including a term for duct friction and explicitly capturing the aspect ratio (9). Noting that freestream velocity v is a function of stage count and the coefficients of drag and friction C_d and C_f are functions of Reynolds number, the utility of this equation is limited without focused aerodynamic measurements.

$$F_N(AR,N,\kappa) = N\frac{I_1(\kappa)d_{ec}}{\mu} - N\frac{1}{2}\rho v^2 C_d A_c(AR) - \frac{1}{2}\rho v^2 C_f S_d(AR,N) \tag{9}$$

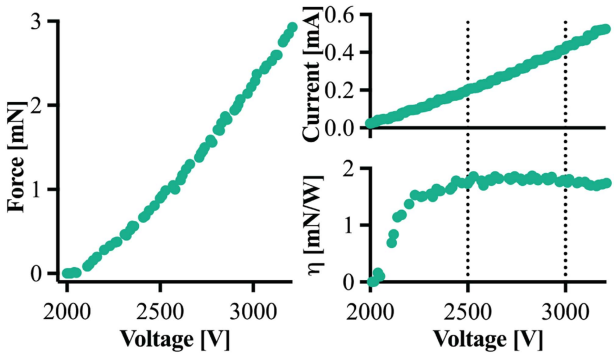

Fig. 18. Characterization of a five-stage aspect ratio five device operated up to approximately 3.3 kV.

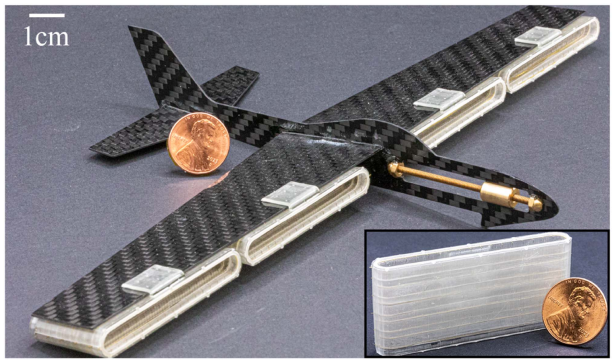

Fig. 19. Proof of concept for a commercial MAV-scale carbon fiber glider with five-stage, aspect ratio nine thrusters mounted underwing along the leading edge. The existing ballast mass seen in the nose of this commercial platform could be replaced by power and control electronics. This prototype is for visualization purposes only and does not yet take flight.

F. Towards Distributed Propulsion

At five stages, the highest tested, an aspect ratio five device achieves a thrust density of 17.93 N/m^2 (3.09 mN output force with 172.27 mm^2 inner area) at 3.28 kV, with an efficiency of 1.86 mN/W (Fig. 18). Compared to state-of-the-art flapping wing platforms, like the DEA-based design presented by Ren et al. [10] with a calculated thrust density of ≈12 N/m^2 and a thrust efficiency of 10 mN/W (and up to 20 mN/W for a higher voltage design), this is a significantly higher thrust density and a significantly lower efficiency (as reflected in Fig. 3). The overall output force exceeds what has been shown from any flapping wing robot if each driven wing is considered separately [10]. It is important to note that the efficiency values derived for flapping wing- and propeller-based fliers include the lift generated by the wings/rotors. Assuming that a lift-to-drag ratio between 5 and 10 is possible for a centimeter-scale MAV [31], our efficiency actually looks promising for a non-VTOL platform.

We hypothesize that the narrow form factor afforded by these high aspect ratio actuators lends itself to distributed propulsion on fixed-wing platforms, where it is important to minimize the impact of the actuator on the aerodynamic performance of the airfoil (i.e., minimize viscous drag [11]). Fig. 19 shows five-stage aspect ratio nine devices integrated under the wing of a commercial MAV-scale glider as a proof-of-concept. The four aspect ratio nine thrusters are expected to produce about 22 mN

of combined force (17.58 N/m^2, 316.27 mm^2 thruster area); with sufficient lift from the wings and modifications to improve thrust-to-weight ratio, that could be sufficient for short power autonomous flight.

V. Conclusion and Future Work

We show that serial integration of multiple acceleration stages in a ducted electroaerodynamic actuator increases thrust density to levels exceeding existing alternatives, and elongating to high aspect ratios increases output force while providing a suitable form factor for distributed propulsion on fixed-wing micro air vehicles. We demonstrate a novel device design with over twice the measured thrust density of any EAD actuator ever measured at this scale ($\approx$18 N/m^2 versus a prior $\approx$7 N/m^2 [12]).

A major limitation of this work is that the duct design was optimized for rapid experimentation with discrete devices, which resulted in a low thrust-to-weight ratio unsuitable for flight. Replacing the SLA-printed ducts with either UV laser micromachined Kapton tubing or two-photon-polymerization printed thin wall structures would drastically reduce mass; we estimate that a thrust-to-weight ratio of over 2.5 is achievable without significant redesign effort.

Thrust efficiency of the demonstated actuators is still too low for use in a power autonomous MAV. In future work, higher stage counts, necessary to increase Reynolds number, could yield efficiency gains through either fluid dynamic (e.g., pressure driven flow out an exhaust nozzle) or aerodynamic (e.g., lift generated by an airfoil intake lip) mechanisms. This may require a redesign of the collector electrode to allow for fully developed flow without grid-induced turbulence. Efficiency should also be assessed as a function of freestream velocity (i.e., in a windtunnel or during free flight) instead of in purely static conditions.

While our investigation explores new parts of the EAD actuator design space and indicates important geometric parameters governing performance, the "correct" design can only be chosen through rigorous multi-objective optimization based on application-specific constraints; we leave this for future work on the design of a power-autonomous flier.

References

[1] D. Floreano and R. J. Wood, "Science, technology and the future of small autonomous drones," *Nature*, vol. 521, no. 7553, pp. 460–466, 2015.

[2] M. Dorigo, G. Theraulaz, and V. Trianni, "Reflections on the future of swarm robotics," *Sci. Robot.*, vol. 5, no. 49, 2020, Art. no. eabe4385.

[3] T. A. Ward, C. J. Fearday, E. Salami, and N. Binti Soin, "A bibliometric review of progress in micro air vehicle research," *Int. J. Micro Air Veh.*, vol. 9, no. 2, pp. 146–165, 2017.

[4] Y. P. Talwekar, A. Adie, V. Iyer, and S. B. Fuller, "Towards sensor autonomy in sub-gram flying insect robots: A lightweight and power-efficient avionics system," in *Proc. IEEE Int. Conf. Robot. Automat.*, 2022, pp. 9675–9681.

[5] J. James, V. Iyer, Y. Chukewad, S. Gollakota, and S. B. Fuller, "Liftoff of a 190 mg laser-powered aerial vehicle: The lightest wireless robot to fly," in *Proc. IEEE Int. Conf. Robot. Automat.*, 2018, pp. 3587–3594.

[6] X. Zhou et al., "Swarm of micro flying robots in the wild," *Sci. Robot.*, vol. 7, no. 66, 2022, Art. no. eabm5954.

[7] Y. Mulgaonkar, M. Whitzer, B. Morgan, C. M. Kroninger, A. M. Harrington, and V. Kumar, "Power and weight considerations in small, agile quadrotors," *Proc SPIE*, vol. 9083, pp. 376–391, 2014.

[8] B. Schäffer, R. Pieren, K. Heutschi, J. M. Wunderli, and S. Becker, "Drone noise emission characteristics and noise effects on humans–a systematic review," *Int. J. Environ. Res. Public Health*, vol. 18, no. 11, 2021, Art. no. 5940.

[9] R. J. Wood et al., "Progress on 'pico'air vehicles," *Int. J. Robot. Res.*, vol. 31, no. 11, pp. 1292–1302, 2012.

[10] Z. Ren et al., "A high-lift micro-aerial-robot powered by low-voltage and long-endurance dielectric elastomer actuators," *Adv. Mater.*, vol. 34, no. 7, 2022, Art. no. 2106757.

[11] H. Xu et al., "Flight of an aeroplane with solid-state propulsion," *Nature*, vol. 563, no. 7732, pp. 532–535, 2018.

[12] D. S. Drew, N. O. Lambert, C. B. Schindler, and K. S. Pister, "Toward controlled flight of the ionocraft: A flying microrobot using electrohydrodynamic thrust with onboard sensing and no moving parts," *IEEE Robot. Automat. Lett.*, vol. 3, no. 4, pp. 2807–2813, Oct. 2018.

[13] L. Pekker and M. Young, "Model of ideal electrohydrodynamic thruster," *J. Propulsion Power*, vol. 27, no. 4, pp. 786–792, 2011.

[14] K. Masuyama and S. R. Barrett, "On the performance of electrohydrodynamic propulsion," *Proc. Roy. Soc. A: Math., Phys. Eng. Sci.*, vol. 469, no. 2154, 2013, Art. no. 20120623.

[15] C. K. Gilmore and S. R. Barrett, "Electrohydrodynamic thrust density using positive corona-induced ionic winds for in-atmosphere propulsion," *Proc. Roy. Soc. A: Math., Phys. Eng. Sci.*, vol. 471, no. 2175, 2015, Art. no. 20140912.

[16] D. S. Drew and S. Follmer, "High force density multi-stage electrohydrodynamic jets using folded laser microfabricated electrodes," in *Proc. IEEE 21st Int. Conf. Solid-State Sensors, Actuators Microsyst.*, 2021, pp. 54–57.

[17] N. Gomez-Vega, A. Brown, H. Xu, and S. R. Barrett, "Model of multi-staged ducted thrusters for high-thrust-density electroaerodynamic propulsion," *AIAA J.*, vol. 61, no. 2, pp. 767–779, 2023.

[18] N. T. Jafferis, E. F. Helbling, M. Karpelson, and R. J. Wood, "Untethered flight of an insect-sized flapping-wing microscale aerial vehicle," *Nature*, vol. 570, no. 7762, pp. 491–495, 2019. [Online]. Available: https://www.nature.com/articles/s41586-019-1322-0

[19] D. S. Drew and K. S. J. Pister, "First takeoff of a flying microrobot with no moving parts," in *Proc. IEEE Int. Conf. Manipulation, Automat. Robot. Small Scales*, 2017, pp. 1–5.

[20] H. K. H. Prasad, R. S. Vaddi, Y. M. Chukewad, E. Dedic, I. Novosselov, and S. B. Fuller, "A laser-microfabricated electrohydrodynamic thruster for centimeter-scale aerial robots," *PLoS One*, vol. 15, no. 4, Apr. 2020, Art. no. e0231362.

[21] H. Zhang, J. Leng, Z. Liu, M. Qi, and X. Yan, "Passive attitude stabilization of ionic-wind-powered micro air vehicles," *Chin. J. Aeronaut.*, vol. 36, no. 7, pp. 412–419, Dec. 2022.

[22] H. Zhang et al., "A centimeter-scale electrohydrodynamic multi-modal robot capable of rolling, hopping, and taking off," *IEEE Robot. Automat. Lett.*, vol. 7, no. 4, pp. 11791–11798, Oct. 2022.

[23] C. Kim, D. Park, K. Noh, and J. Hwang, "Velocity and energy conversion efficiency characteristics of ionic wind generator in a multistage configuration," *J. Electrostatics*, vol. 68, no. 1, pp. 36–41, 2010.

[24] M. Rickard, D. Dunn-Rankin, F. Weinberg, and F. Carleton, "Maximizing ion-driven gas flows," *J. Electrostatics*, vol. 64, no. 6, pp. 368–376, 2006.

[25] E. Moreau and G. Touchard, "Enhancing the mechanical efficiency of electric wind in corona discharges," *J. Electrostatics*, vol. 66, no. 1-2, pp. 39–44, 2008.

[26] J. L. Pereira, *Hover and Wind-Tunnel Testing of Shrouded Rotors for Improved Micro Air Vehicle Design*. College Park, MD, USA: Univ. Maryland, 2008.

[27] V. Hrishikeshavan, J. Black, and I. Chopra, "Design and testing of a quad shrouded rotor micro air vehicle in hover," in *Proc. 53rd AIAA/ASME/ASCE/AHS/ASC Struct., Struct. Dyn. Mater. Conf. 20th AIAA/ASME/AHS Adaptive Struct. Conf. 14th AIAA*, 2012, Art. no. 1720.

[28] D. S. Drew and K. S. Pister, "Geometric optimization of microfabricated silicon electrodes for corona discharge-based electrohydrodynamic thrusters," *Micromachines*, vol. 8, no. 5, 2017, Art. no. 141.

[29] R. Sigmond, "The unipolar corona space charge flow problem," *J. Electrostatics*, vol. 18, no. 3, pp. 249–272, 1986.

[30] L. A. K. Alexander Fridman, *Plasma Physics and Engineering*. Boca Raton, FL, USA: CRC Press, 2014.

[31] R. J. Wood et al., "Design, fabrication and initial results of a 2g autonomous glider," in *Proc. IEEE 31st Annu. Conf. Ind. Electron. Soc.*, 2005, pp. 1–8.